ADVANCED ENERGY MATERIALS
www.advenergymat.de

Check for updates

Isolation of Metalloid Boron Atoms in Intermetallic Carbide Boosts the Catalytic Selectivity for Electrocatalytic N_2 Fixation

Yankun Wen, Zechao Zhuang, Han Zhu, Jiace Hao, Kaibin Chu, Feili Lai,* Wei Zong, Chan Wang, Piming Ma, Weifu Dong, Shuanglong Lu, Tianxi Liu, and Mingliang Du**

The electrochemical N_2 reduction reaction (eNRR) is considered to be an attractive alternative to overcome the short-comings of the Haber-Bosch method, where the electrocatalysts play a vital role in the eNRR efficiency. Herein, isolated single-B sites with electron deficiency in intermetallic carbide are rationally designed to trigger charge density redistribution, achieving excellent selectivity for eNRR. The B-rich VC nanocrystals are in situ synthesized on carbon nanofibers (B-VC/CNFs), and the ordered intermetallic structure of VC can isolate contiguous B atoms into single-B sites with specific electronic structures. In light of density functional theory calculations, the as-designed B—C—V configuration can regulate the adsorption behavior of N_2 and decrease the energy barrier for the proton–electron coupling and transferring process (*NN → *NNH), endowing the distinguished activity and selectivity, as evidenced by excellent Faradaic efficiency of 46.1% and NH_3 yield of 0.443 µmol h^{-1} cm^{-2}. The operando Raman spectra reveals the formation of —NH intermediates on the surfaces of B-VC/CNFs, further confirming the calculated eNRR pathway. This intermetallic carbide host strategy for generating electron-deficient single-B sites offers powerful guidelines for designing advanced eNRR electrocatalysts to achieve effective ammonia production.

1. Introduction

The industrial synthesis of ammonia mainly relies on the Haber-Bosch (H-B) process, which requires high temperature (350–550 °C) and pressure conditions (50–350 atm).[1–3] Up to date, it has become a new research hotspot to produce ammonia through electrochemical nitrogen reduction reaction (eNRR) technology under ambient conditions due to its environmentally friendly characteristics, flexibility, and low cost.[4] The extremely stable N≡N bond, weak N_2 adsorption, and high energy barrier of key intermediates usually require electrocatalysts to improve the eNRR activity and selectivity in ammonia production.[5] However, developing advanced electrocatalysts to improve the eNRR performance with high selectivity is challenging work. Boron-based materials such as boron carbide nanosheets, metal boride, boron nitride, and B-doped carbon have been considered as promising eNRR electrocatalysts.[6–9] Doping engineering and pyrolysis of B-based organic compounds are the two main strategies to generate B active sites.[10,11] Yan groups have demonstrated that boron-rich covalent–organic frameworks could effectively facilitate the N_2 accessibility, achieving a high Faradaic efficiency (FE) of 45.43%.[12] This work shows a sign that increasing the B contents and numbers of B active sites could be an effective approach to improve the eNRR activity and selectivity.

Recently, applying intermetallic compounds to achieve isolated single-atom sites is an important strategy to improve atomic utilization and break the intrinsic activity limit.[13–17] Extensive efforts mainly focus on the metal sites isolation using intermetallic compounds. Few works have reported the non-metal site isolation in intermetallic compounds and these atomic-scale regulations have become a grand challenge. As a special intermetallic compound, vanadium carbide (VC) has high compositional richness and structural diversity that can make the nonmetal C atoms as well as B and N atoms mutually soluble in the VC crystal matrix.[18] The ordered intermetallic structure of VC can isolate contiguous B atoms into single-B sites with specific electronic structures. Rational regulation in

Y. Wen, H. Zhu, J. Hao, K. Chu, C. Wang, P. Ma, W. Dong, S. Lu, T. Liu, M. Du
Key Laboratory of Synthetic and Biological Colloids
Ministry of Education School of Chemical and Material Engineering
Jiangnan University
Wuxi, Jiangsu 214122, P. R. China
E-mail: zhysw@jiangnan.edu.cn; du@jiangnan.edu.cn

Z. Zhuang
Department of Chemistry
Tsinghua University
Beijing 100084, P. R. China

F. Lai
Department of Chemistry
KU Leuven
Celestijnenlaan 200F, Leuven 3001, Belgium
E-mail: feili.lai@kuleuven.be

W. Zong, T. Liu
State Key Laboratory for Modification of Chemical Fibers and Polymer Materials
College of Materials Science and Engineering
Donghua University
Shanghai 201620, China

The ORCID identification number(s) for the author(s) of this article can be found under https://doi.org/10.1002/aenm.202102138.

DOI: 10.1002/aenm.202102138

 © 2021 Wiley-VCH GmbH

electronic structures could effectively favor the N_2 adsorption, activation, and hydrogenation (N_2-AAH) process.[19] The above consideration inspires us to use the VC as a host to generate the high concentration of isolated single B sites and expect superior eNRR performance.

Herein, we demonstrated that boron-rich vanadium carbide with a high concentration of electron-deficient single-B sites could regulate the adsorption behavior of N_2 and decrease the energy barrier for the proton–electron coupling and transferring process (*NN → *NNH), endowing the distinguished activity and selectivity. The boron-rich vanadium carbide (B-VC) were in situ synthesized on carbon nanofibers (CNFs) through the thermodynamic-driven solid-phase diffusion approach by combining the electrospinning technology and high-temperature carbonization. In the B-VC structures, the B and adjacent C bonded with V form the B—C—V bond due to the affinity among the electronegatively weak B, V, and strong C. Both of the B and V atoms donate electrons to C atoms, leading to the redistribution of charge density on V and B sites. The electron-deficient single-B sites with unoccupied p orbitals can enhance the N_2 adsorption and activation. When serving as eNRR electrocatalysts, excellent activity and selectivity with a high ammonia yield of 0.443 μmol h^{-1} cm^{-2} and outstanding FE of 46.1% were realized in 0.5 M K_2SO_4 solution under ambient conditions. In light of density functional theory (DFT) calculations, the as-designed B—C—V configuration can facilitate the electron redistribution that is beneficial for the charge transfer and improve both the activity and selectivity toward eNRR. The operando Raman spectra revealed the formation of —NH intermediates on surfaces of B_{11}-VC/CNFs, further confirming the calculated eNRR pathway.

2. Results and Discussion

To understand the impact of electron-deficient single-B atoms in B—C—V structures with electron redistribution and assess the capability that B-VC catalyzes eNRR, we used DFT calculations to reveal the NRR pathway and corresponding free energy diagrams on B-VC structures. A schematic illustration of the eNRR on B-VC was shown in **Figure 1**a. The optimized V—C and B—C—V models in VC/CNFs and B-VC/CNFs were proposed based on the VC (200) planes. For the active catalytic surface, the (200) facet terminate with V or C termination atoms (B—C—V bonds). According to the Bader charge analysis, in V—C structures, the Bader charge of C atoms bonded with V atoms was –1.29 e (Figure 1b). For the B—C—V structures, due to the smaller electronegativity of B (2.04) than that of C (2.55), the B atoms donated electrons to C atoms, making the Bader charge of C atoms nearby B atoms increased from –1.29 to –1.57 e. Meanwhile, the V atoms nearby the B and C atoms (B—C—V) exhibited a much lower Bader charge relative to the V atoms of the VC structure (Figure 1b). The results revealed that the bridging C atoms received the electron donation from both the B and V atoms, leading to the charge redistribution at B and V atoms. Therefore, these electron-deficient B sites in B—C—V structures can serve as active centers for simultaneously promoting the N_2-AAH process. In addition, the partial density of states (pDOS) of V—C and B—C—V models were shown in Figures S1 and S2 (Supporting Information). Interestingly, both of the two models displayed high density states across the Fermi level, suggesting that the incorporation of B with VC did not weaken the metallic features of VC. This feature also ensured the electron transfers in the subsequent catalytic process for B—C—V models.

We compared the eNRR pathway on B sites of (200) facet in the B—C—V model and V sites of (200) facet in the VC and B—C—V models (Figure 1c, Figures S3 and S4, Supporting Information). The associative reaction process of eNRR pathway showed that the N_2 absorption, activation, and hydrogenation were the vital steps for determining the eNRR performance.[20] Both of the V sites in the V—C and B—C—V models have stronger N_2 adsorption capability than B sites in the B—C—V model. The adsorption energy of N_2 on V sites (0.096 eV) in the B—V—C model was lower than that one B sites (0.346 eV) in the B—C—V model. The free energies of the eNRR steps were calculated and shown in Figure 1d. The Gibbs free energy diagrams showed that the first N_2 hydrogenation to form *NNH intermediates was the potential determining step (PDS). For V sites in the B—C—V model, the first N_2 hydrogenation to form *NNH needed to overcome an energy barrier (ΔG_{PDS}) of 1.624 eV, which was much higher than that on B sites in B—C—V (0.984 eV). The results revealed that the B sites in B—C—V became the real active sites for promoting the first N_2 protonation to form *NNH and significantly reducing the energy barrier of PDS for eNRR. Therefore, in the whole eNRR pathway, the B sites in B—C—V achieved the lower energy barrier for N_2-AAH processes (N_2 absorption, activation, and hydrogenation) than those of V sites in B—C—V. These results strongly demonstrated that the designed B—C—V structures with electron-deficient B centers simultaneously promote the activation of N_2 and reduction of ΔG_{PDS} for eNRR.

To verify the prediction of the DFT calculations, the B-rich vanadium carbide supported on carbon nanofibers with different B contents (B_x-VC/CNFs, $0 \leq x \leq 15$) were synthesized through a thermodynamic-driven solid-phase diffusion approach by combining the electrospinning technology and high-temperature carbonization (see details in Supporting Information).[21–23] Briefly, as shown in **Figure 2**a, the boric acid and acetylacetonate vanadium (H_3BO_3 and $C_{10}H_{14}O_5V$) were firstly homogeneous dissolved in the polyacrylonitrile/*N*, *N*′-dimethylformamide (PAN/DMF) solution. The H_3BO_3, $C_{10}H_{14}O_5V$, and PAN were used as B, V, and C sources, respectively. Then, the B and V salt/PAN precursor nanofiber membrane was obtained through the electrospinning process. After the graphitization at 1000 °C, the B-VC/CNFs with unique B—C—V structures were finally produced. The intermetallic compound vanadium carbide exhibits the superior B contents and by adjusting the mass ratios of B and V salts, the B-VC/CNFs with various B contents (B atom ratio = 0, 3, 5, 8, 11, and 15 at%) were prepared. Their chemical formulas were denoted as VC/CNFs, B_3-VC/CNFs, B_5-VC/CNFs, B_8-VC/CNFs, B_{11}-VC/CNFs, and B_{15}-VC/CNFs, respectively. The elemental composition was investigated by the energy-dispersive X-ray spectra (EDS) (Table S1, Supporting Information).

The morphologies of the B_{11}/CNFs, VC/CNFs, and B_{11}-VC/CNFs hybrids were investigated by field emission scanning

© 2021 Wiley-VCH GmbH

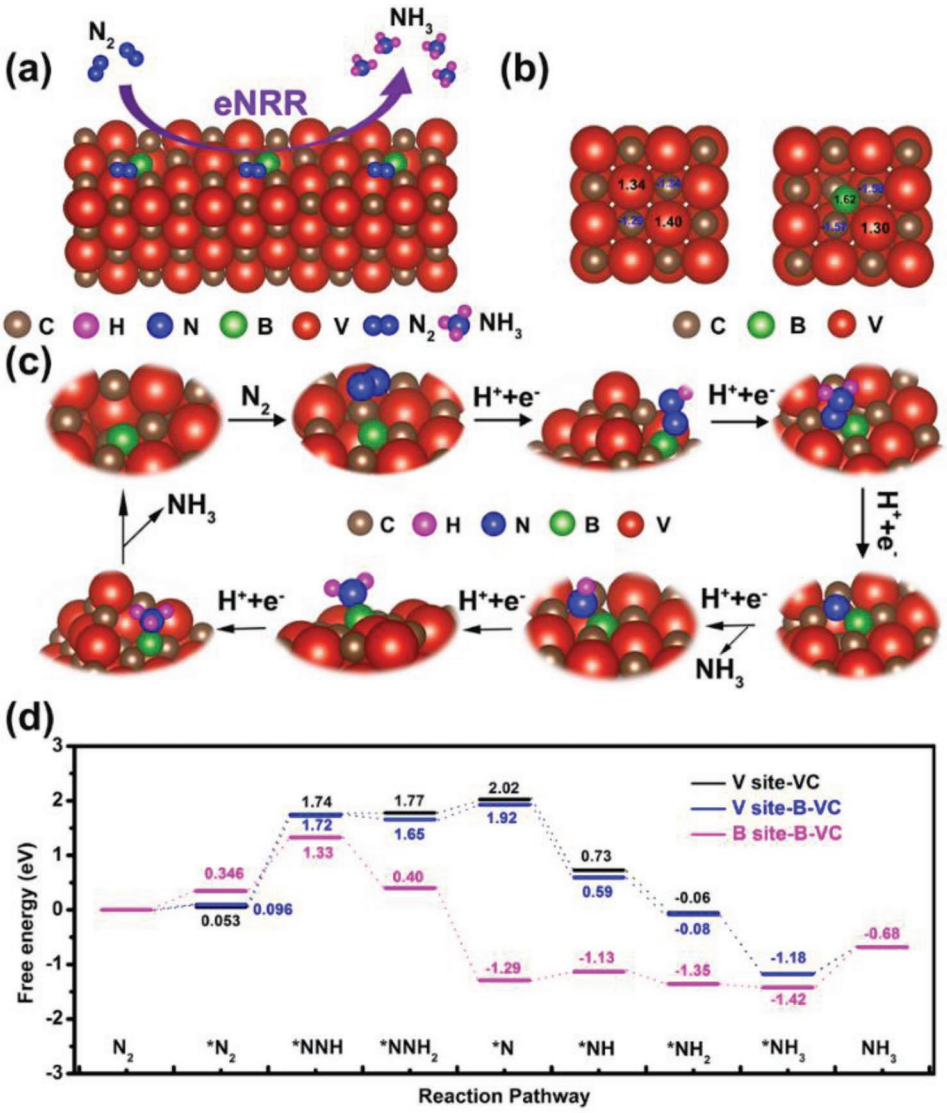

Figure 1. a) Schematic illustration of the eNRR on B-VC. b) Charge distribution on VC model and B-VC model. c) DFT-calculated eNRR reaction cycle through distal pathway on the B site in B-VC model. d) Free energy diagrams of distal eNRR pathway on the V site of VC, V site of B-VC, and B site of B-VC.

electron microscopy (FESEM) and transmission electron microscopy (TEM). The B_{11}/CNFs (Figure S5a, Supporting Information), VC/CNFs (Figure S5b, Supporting Information), and B_{11}-VC/CNFs (Figure 2b) all displayed distinct nanofiber morphologies with random distributions to form the unique three-dimensional (3D) network architectures. The B_{11}/CNFs exhibited a smooth surface (Figure S5c, Supporting Information) while both of the VC/CNFs (Figure S5d, Supporting Information) and B_{11}-VC/CNFs (Figure 2c) indicated that plenty of small nanocrystals were distributed on the substrate CNFs homogeneously without obvious aggregation. High-angle annular dark field scanning TEM (HADDF-STEM) images of B_{11}-VC/CNFs (Figure 2d) demonstrated that the diameter of B_{11}-VC nanocrystals ranged from 5 to 10 nm while the size of CNFs varied from 150 to 300 nm. The high-resolution TEM image of B_{11}-VC/CNFs (Figure 2e) displayed the nanoparticles were crystallized with the interplanar spacing of 2.1 Å, corresponding to the (200) planes of VC.

The HAADF-STEM image (Figure 2f) and STEM electron energy loss spectrum (STEM-EELS) mapping images (Figure 2g–i) of the B_{11}-VC nanoparticles supported on CNFs revealed the uniform distribution of the C, B, and V elements. STEM-EELS spectrum was recorded on the surface of B_{11}-VC nanocrystal (Figure 2j). The EELS spectrum revealed the presence of the K edges for C and B and L edges for V, respectively. The energy-loss near-edge structure (ELNES) of the C K-edge showed a well-defined graphitic character with a π^* peak at 285 eV and a detailed σ^* structure above 295 eV.[24] When compared with the π^* peak of B elementary substance (188 eV), the π^* peak in B K-edge of B_{11}-VC shifted to 192 eV, indicating the presence of B-C bonds.[25] The ELNES of V $L_{2,3}$-edges showed peaks at 524 and 517 eV, corresponding to the signals from the

© 2021 Wiley-VCH GmbH

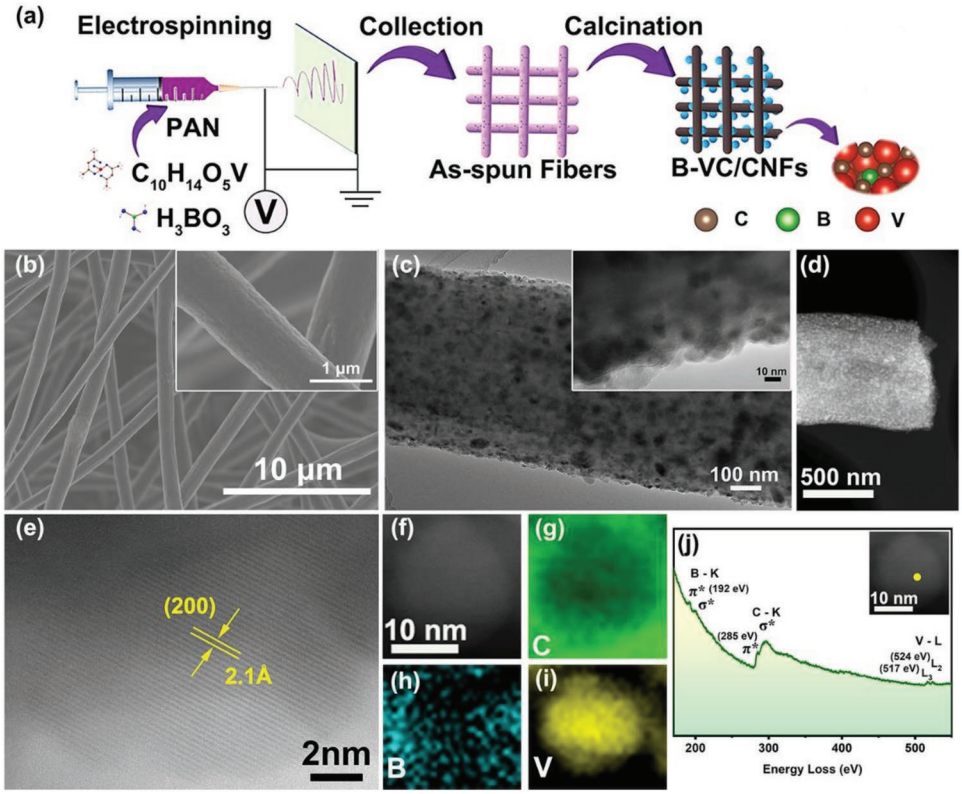

Figure 2. a) Schematic diagram for the fabrication procedures of B_x-VC supported on CNFs (B_x-VC/CNFs, $0 \leq x \leq 15$). b) FESEM and c) TEM images of B_{11}-VC/CNFs hybrid. Insets in Figure 1b,c are the corresponding high-magnification images. d) HAADF-STEM image of the B_{11}-VC/CNFs hybrid. e) HRTEM image of a B_{11}-VC nanocrystal supported on CNFs. f–i) STEM-EELS mapping images of the B_{11}-VC/CNFs. j) Typical STEM-EELS spectrum obtained from a randomly selected spot on the surface of B_{11}-VC nanocrystal supported on CNFs. Inset is the corresponding investigated B_{11}-VC nanocrystal.

vanadium valence state of +4.[26] Therefore, the EELS evidence confirmed that B atoms were successfully incorporated into the VC crystal matrix, forming the B—C—V structures.

Typical X-ray diffraction (XRD) patterns of VC/CNFs and B_{11}-VC/CNFs were shown in **Figure 3**a,b. A broad band around 22° was assigned to the amorphous carbon of CNFs. A series of peaks were well indexed to the (111), (200), (220), (311), and (222) planes of cubic VC phase (JCPDS No. 73-0476).[27] Interestingly, the enlarged XRD patterns in Figure 3b indicate the slightly shifts (0.18° of 2θ) in peak positions of the (111) and (200) planes for the VC and B_{11}-VC phases, demonstrating that the B incorporation into the VC crystal lattice can lead to enlarged V—C lattices.

X-ray photoelectron spectroscopy (XPS) was used to investigate the chemical states of VC/CNFs and B_{11}-VC/CNFs. All the binding energies (BEs) were calibrated by the C 1s peak at 284.6 eV. The B 1s spectra of VC/CNFs without B doping exhibited no B signals (Figure 3c). Meanwhile, the B 1s XPS spectra of B_{11}-VC/CNFs can be fitted by four distinct peaks at 189.9, 190.4, 191.2, and 192.3 eV, corresponding to BC_3, B—C—V, BC_2O, and BCO_2 species, respectively (Figure 3c).[28] The B XPS spectra strongly demonstrated the successful formation of B-C and B—C—V bonds in B_{11}-VC/CNFs. The atomic concentration of B was determined to be 11.2 at% via XPS spectra, which was well matched with the EDS results (Table S1, Supporting Information). Figure 3d revealed the typical C 1s spectra of VC/CNFs and B_{11}-VC/CNFs. The VC/CNFs displayed three main peaks at 282.0, 284.6, and 286.3 eV corresponding to the C—V, C—C, and C—O bonds, respectively.[29] Meanwhile, the B_{11}-VC/CNFs exhibited four main peaks at 282.2, 284.3, 284.6, and 286.3 eV, which were ascribed to the B—C—V, C—B, C—C, and C—O bonds, respectively. Due to the incorporation of B into V—C, the BE of B—C—V bonds (282.2 eV) in B_{11}-VC/CNFs exhibited a positive shift of 0.2 eV when compared with the BE (282.0 eV) of C—V bonds in VC/CNFs, suggesting the electron donation from V and B atoms to C atoms. The V 2p spectra of VC/CNFs can be deconvoluted into six peaks (Figure 2e), which were attributed to the V^{2+} (513.7 and 520.9 eV), V^{3+} (515.3eV and 525.1 eV), and V^{4+} (516.8 and 523.7 eV), respectively.[30] Furthermore, the BEs of V^{4+} for B_{11}-VC/CNFs shifted to the relatively high values of 516.6 and 523.5 eV, also indicating that the V atoms tended to donate electrons to C atoms. The results indicated that the formation of B—C—V bonds leads to the enhanced electron transfers among the V, B, and C atoms.

Temperature-programmed desorption (TPD) was further used to investigate the N_2 adsorption capacity of VC/CNFs and B_{11}-VC/CNFs.[31] As shown in Figure 3f, both of the VC/CNFs and B_{11}-VC/CNFs showed two obvious peaks in the range of 100–600 °C, which can be attributed to the physical and chemical adsorption of N_2 molecules on the surface of catalysts, respectively. Interestingly, the peak intensity of the chemisorption peak of B_{11}-VC/CNFs at about 530 °C was significantly

© 2021 Wiley-VCH GmbH

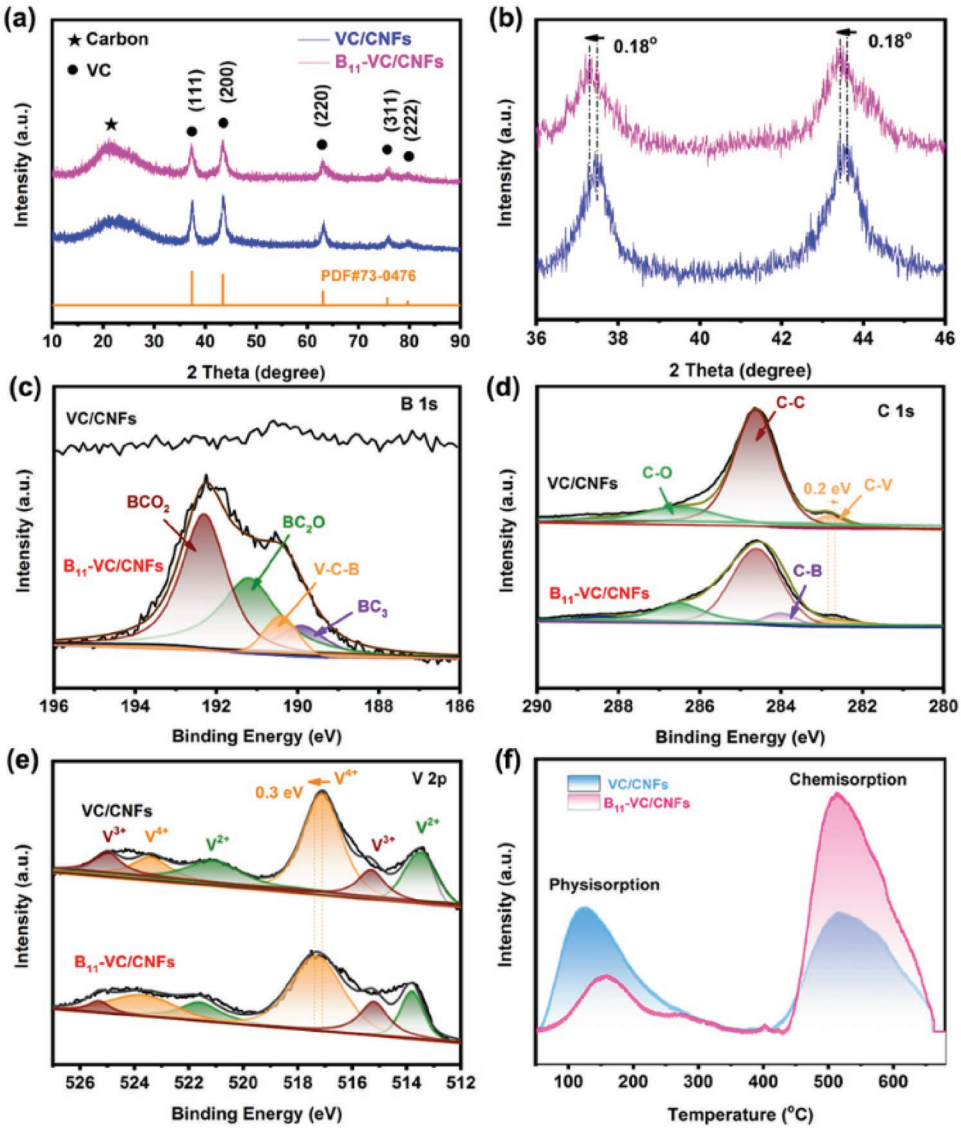

Figure 3. a,b) XRD patterns of VC/CNFs and B_{11}-VC/CNFs. c) B 1s, d) C 1s, and e) V 2p XPS spectra of VC/CNFs and B_{11}-VC/CNFs. f) N_2 TPD curves of VC/CNFs and B_{11}-VC/CNFs.

stronger than that of VC/CNFs. The N_2-TPD results indicate that the formation of B—C—V significantly enhanced the chemical adsorption capacity of N_2, which would lead to the enhanced eNRR performance.

The eNRR activity of as-prepared catalysts was performed in an H-type cell with a typical three-electrode system in 0.5 M K_2SO_4 solution under continuous N_2 flow. In the H-type cell, the Ag/AgCl reference electrode was placed in the cathode chamber while the platinum wire counter electrode was placed in the anodic chambers. The cathode chamber and anodic chambers were separated by the commercial Nafion 117 membrane. All the as-prepared samples were employed as cathodes for eNRR. The B_{11}-VC/CNFs membrane with an electrode area of 0.25 cm^2 (0.5 × 0.5 cm) was fixed on a Teflon motor clip as the working electrode. During the eNRR process, N_2 pretreated with an acid solution was continuously provided to the cathode. The H^+ in the electrochemical cell transported through the 0.5 M K_2SO_4 electrolyte and reacted with N_2 on the catalyst surface for NH_3 production. The possible eNRR products in the 0.5 M K_2SO_4 electrolyte were NH_3 and N_2H_4, respectively. The NH_3 product was determined by the indophenol blue method (Figure S6, Supporting Information), and the byproduct N_2H_4 was detected by the Watt-Christo method (Figure S7, Supporting Information). As shown in Figure S8 (Supporting Information), the UV–vis spectra indicate that no N_2H_4 byproduct was detected, suggesting that the reaction on B_{11}-VC/CNFs gives excellent selectivity for NH_3 production. The eNRR activity of B_{11}-VC/CNFs was initially evaluated by linear sweep voltammetry (LSV) polarization curves in the N_2- and Ar-saturated 0.5 M K_2SO_4 electrolytes (Figure S9, Supporting Information). The LSV curve in the N_2-saturated electrolyte exhibited enhanced current density relative to that in the Ar-saturated electrolyte, suggesting that the B_{11}-VC/CNFs was certainly active for the eNRR. Moreover, in the potential window

© 2021 Wiley-VCH GmbH

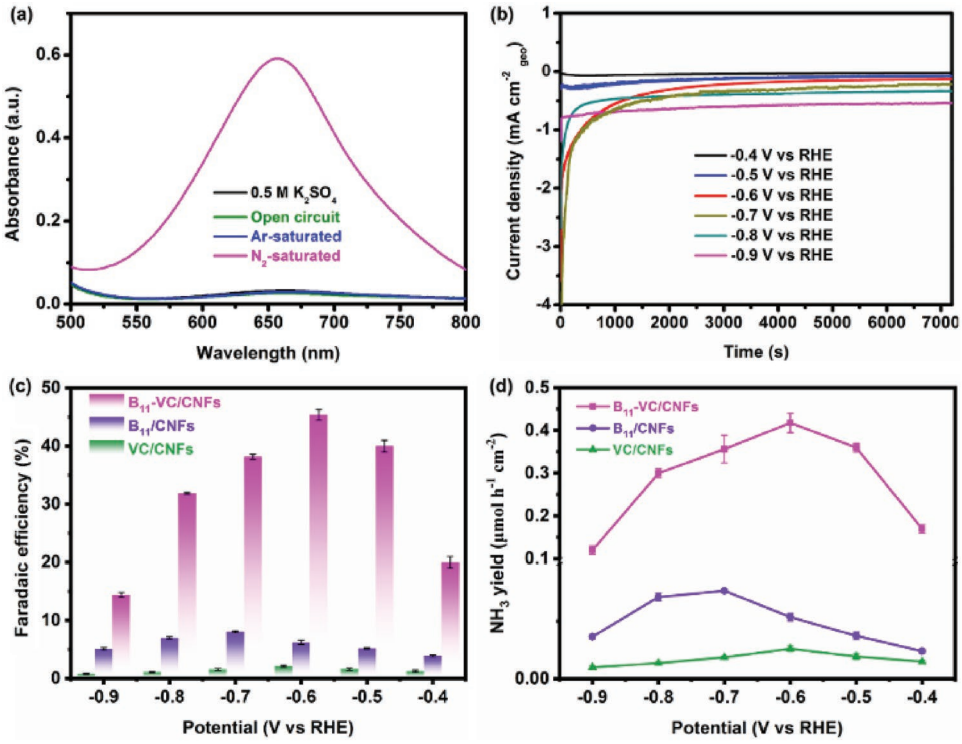

Figure 4. a) UV–vis absorption spectra of initial 0.5 M K_2SO_4, N_2-saturated 0.5 M K_2SO_4 catalyzed by B_{11}-VC/CNFs under open circuit, N_2-saturated 0.5 M K_2SO_4, and Ar-saturated 0.5 M K_2SO_4 catalyzed by B_{11}-VC/CNFs at –0.6 V versus RHE. b) Chronoamperometry curves of B_{11}-VC/CNFs at various potentials for 2 h in N_2-saturated 0.5 M K_2SO_4. Comparison in c) FEs and d) NH_3 yields of B_{11}-VC/CNFs, VC/CNFs, and B_{11}/CNFs at each given potential in N_2-saturated 0.5 M K_2SO_4.

from –0.4 to –0.8 V, a significantly higher current density was achieved in the N_2-saturated electrolyte than that in the Ar-saturated electrolyte. Therefore, the potential window from –0.4 to –0.8 V was selected for the eNRR. The electrochemical active surface area (ECSA) was determined based on the electrochemical double-layer capacitance (C_{dl}). The B_{11}-VC/CNFs obtained the highest C_{dl} value of 13.2 mF cm^{-2} relative to those of VC/CNFs (8.3 mF cm^{-2}) and B_{11}/CNFs (1.5 mF cm^{-2}), respectively, indicating the high intrinsic activity of B_{11}-VC/CNFs (Figure S10, Supporting Information).

A series of control experiments were used to investigate the effect of N_2 as the N source and eliminate the interferences of contaminants in the testing system (**Figure 4**a). Specifically, no ammonia was detected in the initial N_2-saturated 0.5 M K_2SO_4 electrolyte and the electrolyte catalyzed by B_{11}-VC/CNFs under open-circuit potential. These experiments can rule out the effect of contamination in the N_2 gas flow and the B_{11}-VC/CNFs itself. In the Ar atmosphere, the UV–vis spectra show negligible absorption peak while a strong absorption peak can be observed in the N_2 atmosphere, suggesting the production of NH_3 catalyzed by B_{11}-VC/CNFs during the eNRR process. These results demonstrated that the detected ammonia was only produced from the eNRR process. The eNRR activities of B_{11}-VC/CNFs were quantified via chronoamperometry measurements at different potentials for 2 h (Figure 4b). The current density increased with the potentials ranged from –0.4 to –0.9 V. To investigate the contributions of the B—C, VC, and B—C—V structures for the eNRR performance, the B_{11}/CNFs with BC_3 structures were also prepared at the same condition. We performed a variety of comparative experiments to eliminate the influencing factors on NRR activity. Figure 4c,d shows the corresponding Faradaic efficiencies (FE) and NH_3 yields of B_{11}/CNFs, VC/CNFs, and B_{11}-VC/CNFs catalysts at each potential. The FE and NH_3 yield on VC/CNFs exhibit negligible values, and the B_{11}/CNFs with BC_3 structures display the FE of 8.4% and the NH_3 yield of 0.062 μmol h^{-1} cm^{-2} at –0.7 V versus RHE. The results indicated that without the B incorporation, the pure VC had little effect on NRR activity. In comparison, the B_{11}-VC/CNFs with B—C—V bonds reached a maximum FE of 46.1% and an NH_3 yield of 0.443 μmol h^{-1} cm^{-2} at –0.6 V versus RHE, which was significantly higher than the reported level in the literature (Table S2, Supporting Information).

We have further explored the influences of B contents on the eNRR performances. As shown in Figure S11a,b (Supporting Information), with the increased B contents, the FEs and NH_3 yields of the as-synthesized B_x-VC/CNFs electrocatalysts displayed an escalating trend due to the increased numbers of B active sites in B—C—V. However, when the B contents increased to 15%, the B_{15}-VC/CNFs exhibited decreased FE of 34.1% and NH_3 yield of 0.275 μmol h^{-1} cm^{-2}. The results demonstrated that except for the B—C—V active sites, the additionally formed BC_3 structures in B_{15}-VC/CNF could not afford the high eNRR activity, further confirming that the eNRR activity was determined by B—C—V structures in B-VC/CNFs. Therefore, the main contribution in B_{11}-VC/CNFs for eNRR was attributed to the unique B—C—V structures, which can regulate

© 2021 Wiley-VCH GmbH

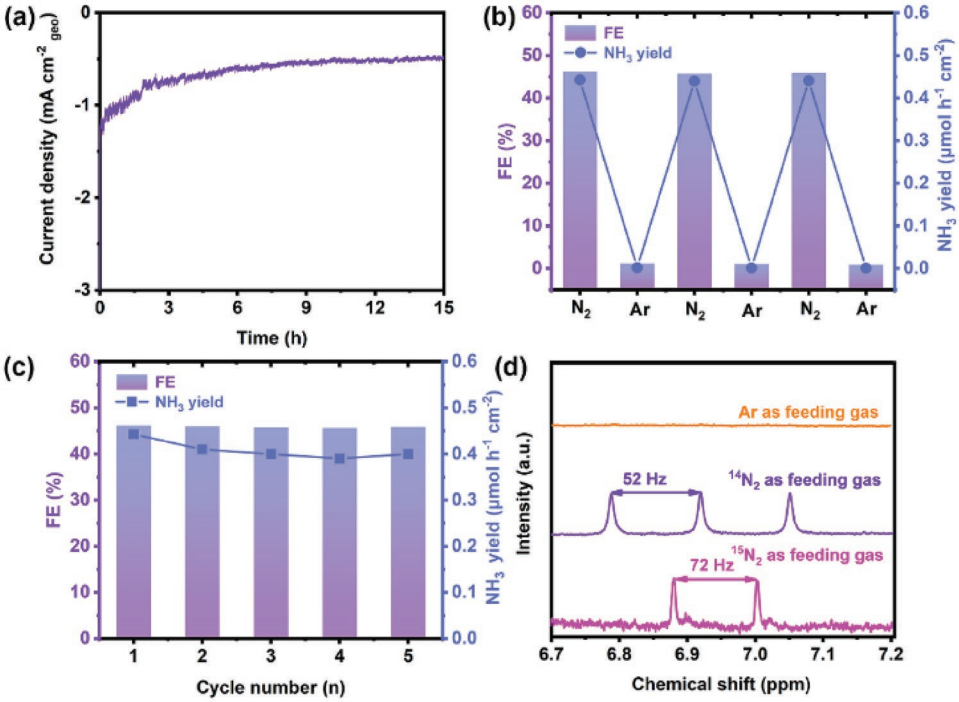

Figure 5. a) Chronoamperometry test of B_{11}-VC/CNFs under continuous NRR electrolysis for 15 h. b) FEs and the corresponding NH_3 yields of B_{11}-VC/CNFs performed at –0.6 V versus RHE by alternating Ar-saturated and N_2-saturated 0.5 M K_2SO_4. c) NH_3 yields and the corresponding FEs of B_{11}-VC/CNFs obtained at –0.6 V versus RHE during five-time cycles for NRR in N_2-saturated 0.5 M K_2SO_4. d) ^{1}H NMR spectra of electrolytes after NRR electrolysis on B_{11}-VC/CNFs using $^{14}N_2$, $^{15}N_2$, and Ar as feed gases.

the adsorption behavior of N_2 and reduce the energy barrier of rate-determining steps.

The important stability of the catalyst was investigated by various characterization tests. The time–current curves performed at –0.60 V versus RHE (**Figure 5**a) exhibited a negligible decrease in current density during the 15 h long-term electrolysis experiment. After long-term stability tests, the B_{11}-VC/CNFs still maintained the uniform nanofiber morphology with 3D architecture (Figure S12a,b, Supporting Information), crystal phase (Figure S12c, Supporting Information), and chemical composition and states (Figure S12d, Supporting Information), confirming the excellent stability. In addition, the FE and NH_3 yield before and after 15 h long-term electrolysis was not substantially reduced (Figure S13, Supporting Information). Furthermore, we continuously cycled the NRR test at –0.6 V versus RHE by changing the feeding gas (Ar and N_2) in 0.5 M K_2SO_4 (Figure 5b) and the FEs and NH_3 yields were calculated for each experiment. The results demonstrate that FE (46.1%) and NH_3 yield (0.443 μmol h^{-1} cm^{-2}) of B_{11}-VC/CNFs can be well maintained during each cycle in N_2-saturated electrolyte. We further continuously performed the cycle tests five times in N_2-saturated 0.5 M K_2SO_4 and the B_{11}-VC/CNFs catalyst still maintained efficient eNRR activity (FE of 46.1% and NH_3 yield of 0.443 μmol h^{-1} cm^{-2}) after continuously five cycles, confirming that the B_{11}-VC/CNFs has superior stability.

The NH_3 production was further verified by nuclear magnetic resonance (NMR) using the isotope labeling method with $^{14}N_2$ and $^{15}N_2$ as feeding gases. As shown in Figure 5d, when $^{15}N_2$ was utilized as a nitrogen source, the ^{1}H NMR exhibit distinct doublet with a chemical shift of 72 Hz, which was ascribed to $^{15}NH_4^+$. For $^{14}N_2$ used as the nitrogen source, three signal peaks with a chemical shift of 52 Hz were attributed to $^{14}NH_4^+$.[32] In addition, the calculated FEs and NH_3 yields using NMR were almost consistent with the calculation by colorimetry (Figure S14, Supporting Information). When the Ar was introduced as feeding gas, there was no ammonia signal displayed in NMR spectra. The results proved that the detected ammonia was produced during the eNRR process catalyzed by B_{11}-VC/CNFs, eliminating the effects of NH_3 or NO_3^- contaminants.

To understand the reasons for achieving the high selectivity for NH_3 by B-VC, the capability of B—C—V to suppress the competitive HER was further revealed by the DFT calculations. The differences between the eNRR limiting potential and the competitive HER limiting potential are vital descriptors for eNRR selectivity (**Figure 6**a).[33] The limiting potential (U_L) can be defined as the lowest negative potential at which all basic steps are exergonic. The catalytic activity for HER at the B site and V site in B—V—C and V—C models can be assessed by the calculated Gibbs free energy of hydrogen adsorption (Figure S15, Supporting Information). It can be seen that the B sites in B—C—V models have the relatively stronger hydrogen adsorption capability (0.19 eV) than V sites in B—C—V (0.78 eV) and V—C (0.67 eV) models. Compared with V sites, although the U_L(HER) of B sites is slightly smaller, it has more positive [U_L(NRR) – U_L(HER)] values, suggesting that the B sites in the B—C—V model possess distinguished NRR activity and selectivity.

The projected-crystal orbital Hamilton population (pCOHP) was carried to analyze the interaction between the activity center and the nitrogen adatom.[34] The integrated-crystal OHP

© 2021 Wiley-VCH GmbH

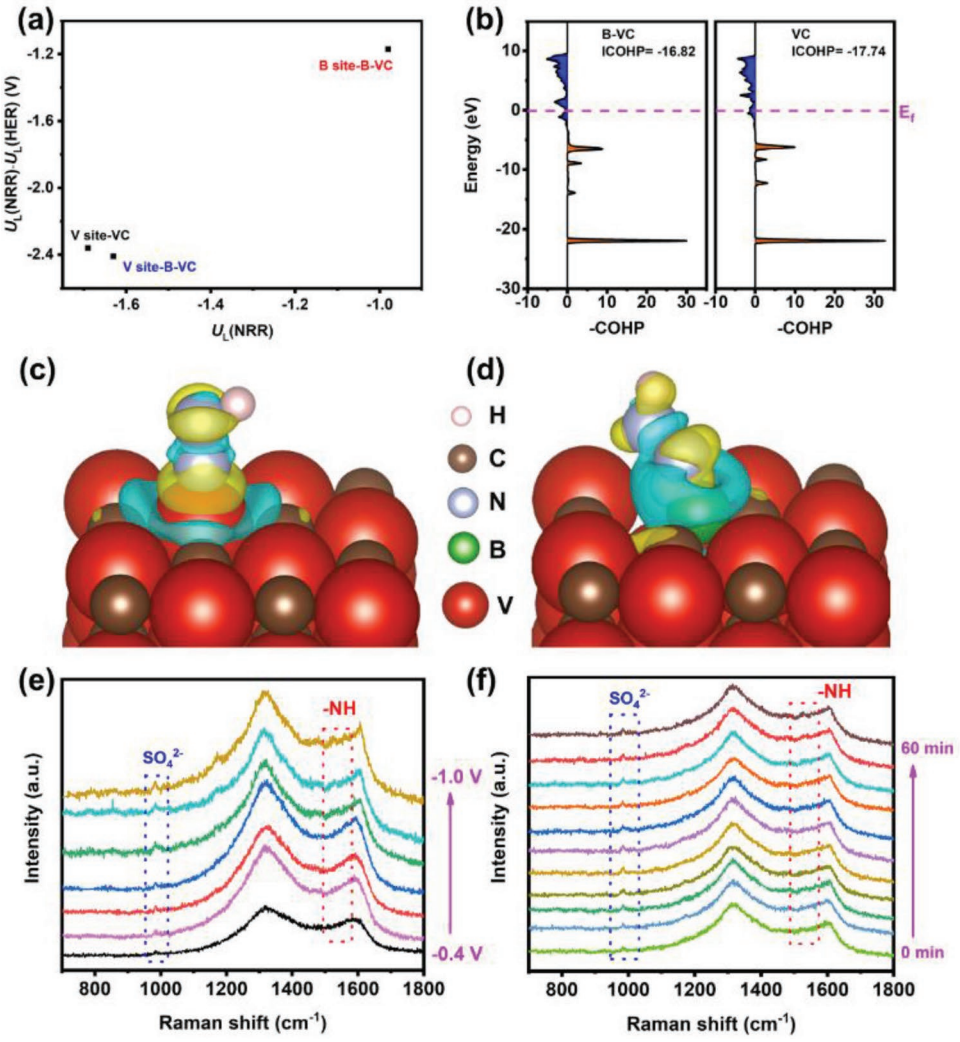

Figure 6. a) Plots of U_L(NRR)–U_L(HER) versus U_L(NRR) illustrating the NRR performance of V site of VC, V site of B-VC, and B site of B-VC. b) Projected crystal orbital Hamilton population (pCOHP) between the metal center VC and B-VC as well as the nitrogen adatom. c) Charge density difference of *NNH configuration at VC. d) Charge density difference of *NNH configuration at B-VC. e) In situ Raman spectra of the B_{11}-VC/CNFs at different applied potential from –0.4 to –1.0 V versus RHE. f) Time-resolved in situ Raman spectra of B_{11}-VC/CNFs collected at –0.6 V versus RHE under a N_2 atmosphere for 1 h.

(ICOHP) analysis of the N≡N bond was performed to investigate the activation degree for N_2 molecules (Figure 6b). In general, the activation degree of N_2 molecules was negatively correlated with the values of ICOHP. The ICOHP values followed the order: V—C model (–17.74) < B—C—V model (–16.82), suggesting that the activation degree of the N≡N bond by B—C—V was stronger than that by V—C. To further investigate the influences of the electron-deficient B sites and V sites on regulating the adsorption behavior of *NNH intermediate, the charge density difference of the *NNH state configuration at VC and B-VC models were shown in Figure 6c,d. The results demonstrate that the electron transfer from B—C—V to the *NNH intermediate was 11.66 eV, which was higher than that from V—C (11.25 eV) to *NNH intermediate, suggesting the stronger electron interaction between B—C—V and the *NNH intermediate.[35] The designed B—C—V can simultaneously promote the formation of *NNH intermediates and stabilize them on B sites.

In situ Raman spectroscopy was further used to monitor the possible reaction intermediates or products on VC/CNFs (Figure S16, Supporting Information) and B_{11}-VC/CNFs (Figure 6e) during the eNRR operation at different potentials in a N_2-saturated 0.5 M K_2SO_4 electrolyte. As shown in Figure S13 (Supporting Information), with the increased applied potential from –0.4 to –1.0 V versus RHE, a Raman peak appeared at 981 cm^{-1}, assigned to the sulfate radical species absorbed on the surface of VC/CNFs, suggesting the excellent wettability for the electrolyte.[36] For the B_{11}-VC/CNFs as electrocatalysts (Figure 6e), under applied potential from –0.4 to –0.5 V versus RHE, a new Raman peak emerged at 1525 cm^{-1}, ascribed to the —NH, demonstrating the strong nitrogen reduction on B_{11}-VC/CNFs. Time-resolved in situ Raman spectra of B_{11}-VC/CNFs collected at –0.6 V versus RHE under a N_2 atmosphere for 1 h were shown in Figure 6f. Besides the Raman peaks at 981 cm^{-1} for sulfate radical species, the Raman peaks at 1525 cm^{-1} for

© 2021 Wiley-VCH GmbH

—NH gradually emerged and enhanced as the eNRR progressed. No such Raman peak at 1525 cm^{-1} was detected for VC/CNFs, suggesting their unfavored NRR performances.[37] The Raman results demonstrate the formation of —NH intermediates on surfaces of B_{11}-VC/CNFs, further confirming the calculated eNRR pathway and the excellent eNRR performance of B_{11}-VC/CNFs. Thus, we have theoretically and experimentally demonstrated that applying the intermetallic compounds VC as host to create high contents of electron-deficient B sites make the enhanced eNRR selectivity and activity by regulating the adsorption behavior of N_2 and decreasing the energy barrier for the proton–electron coupling and transferring process.

3. Conclusion

In summary, we have designed the electron-deficient single-B sites in B-rich VC nanocrystals supported on CNFs by combining the electrospinning technology and carbonization process. DFT calculations demonstrated the charge redistribution over the B—C—V structures. The B—C—V structures with electron-deficient B sites simultaneously can boost the activation of N_2 and reduce the energy barrier of PDS for eNRR. The B_{11}-VC/CNFs exhibited an excellent FE of 46.1% and NH_3 yield of 0.443 μmol h^{-1} cm^{-2} at –0.6 V versus RHE. This intermetallic carbide host strategy offers powerful guidelines for achieving effective ammonia production by generating the electron-deficient dual active centers. The operando Raman spectra demonstrated that the B—C—V is the absorption sites for —NH intermediates in the eNRR progress. This intermetallic carbide host strategy for generating the electron-deficient B active centers offers powerful guidelines for designing advanced eNRR electrocatalysts to achieve effective ammonia production.

Supporting Information

Supporting Information is available from the Wiley Online Library or from the author.

Acknowledgements

Y.W. and Z.Z. contributed equally to this work. This study was supported by the National Natural Science Foundation of China (NSFC) (Grant Nos. 52073124, 51803077), Natural Science Foundation of Jiangsu Province (Grant No. BK20180627), Postdoctoral Science Foundation of China (2018M630517, 2019T120389), the MOE and SAFEA, 111 Project (B13025), the Fundamental Research Funds for the Central Universities, and the Postgraduate Research and Practice Innovation Program of Jiangsu Province (KYCX21-2010). The authors also thank the characterizations supported by Central Laboratory, School of Chemical and Material Engineering, Jiangnan University.

Conflict of Interest

The authors declare no conflict of interest.

Data Availability Statement

Research data are not shared.

Keywords

electrochemical N_2 reduction, electron redistribution, electrospinning, intermetallic compounds, single-B sites

Received: July 14, 2021
Revised: August 10, 2021
Published online:

[1] M. Van Damme, L. Clarisse, S. Whitburn, J. Hadji-Lazaro, D. Hurtmans, C. Clerbaux, P. F. Coheur, *Nature* **2018**, *564*, 99.
[2] T. Spatzal, K. A. Perez, O. Einsle, J. B. Howard, D. C. Rees, *Science* **2014**, *345*, 1620.
[3] B. Ma, J. Liang, T. Li, Q. Liu, Y. Luo, S. Lu, A. M. Asiri, D. Ma, X. P. Sun, *Nano Res.* **2021**, *14*, 555.
[4] Z. Du, J. Liang, S. Li, Z. Xu, T. Li, Q. Liu, Y. Luo, F. Zhang, Y. Liu, Q. Kong, X. Shi, B. Tang, A. M. A. , B. Li, X. P. Sun, *J. Mater. Chem. A* **2021**, *9*, 13861.
[5] T. W. Wu, Z. L. Xing, S. Mou, C. B. Li, Y. X. Qiao, Q. Liu, X. J. Zhu, Y. L. Luo, X. F. Shi, Y. N. Zhang, X. P. Sun, *Angew. Chem., Int. Ed.* **2019**, *58*, 18449.
[6] C. W. Liu, Q. Y. Li, J. Zhang, Y. G. Jin, D. Macfarlane, C. H. Sun, *J. Phys. Chem. C* **2018**, *122*, 25268.
[7] S. X. Li, Y. Y. Wang, J. Liang, T. Xu, D. W. Ma, Q. Liu, T. S. Li, S. R. Xu, G. Chen, A. M. Asiri, Y. L. Luo, Q. Wu, X. P. Sun, *Mater. Today Phys.* **2021**, *18*, 100396.
[8] S. Zhou, X. W. Yang, X. Xu, S. X. Dou, Y. Du, J. J. Zhao, *J. Am. Chem. Soc.* **2020**, *142*, 308.
[9] Y. K. Wen, H. Zhu, J. C. Hao, S. L. Lu, W. Zong, F. L. Lai, P. M. Ma, W. F. Dong, T. X. Liu, M. L. Du, *Appl. Catal., B* **2021**, *292*, 120144.
[10] M. A. Légaré, C. Pranckevicius, H. Braunschweig, *Chem. Rev.* **2019**, *119*, 8231.
[11] M. A. Légaré, G. Bélanger-Chabot, R. D. Dewhurst, E. Welz, I. Krummenacher, B. Engels, H. Braunschweig, *Science* **2018**, *359*, 896.
[12] S. Liu, M. Wang, T. Qian, H. Ji, J. Liu, C. Yan, *Nat. Commun.* **2019**, *10*, 3898.
[13] Q. C. Feng, S. Zhao, Y. Wang, J. C. Dong, W. X. Chen, D. S. He, D. S. Wang, J. Yang, Y. M. Zhu, H. L. Zhu, L. Gu, Z. Li, Y. X. Liu, R. Yu, J. Li, Y. D. Li, *J. Am. Chem. Soc.* **2017**, *139*, 7294.
[14] Y. Nakaya, J. Hirayama, S. Yamazoe, K. I. Shimizu, S. Furukawa, *Nat. Commun.* **2020**, *11*, 2838.
[15] Y. Han, Y. Xiong, C. Liu, H. W. Zhang, M. Q. Zhao, W. Chen, W. X. Chen, W. Huang, *J. Catal.* **2021**, *396*, 351.
[16] S. Chen, Z. J. Zhao, R. T. Mu, X. Chang, J. Luo, S. C. Purdy, A. J. Kropf, G. D. Sun, C. L. Pei, J. T. Miller, X. H. Zhou, E. Vovk, Y. Yang, J. L. Gong, *Chem* **2021**, *7*, 387.
[17] A. J. Han, J. Zhang, W. M. Sun, W. X. Chen, S. L. Zhang, Y. H. Han, Q. C. Feng, L. R. Zheng, L. Gu, C. Chen, Q. Peng, D. S. Wang, Y. D. Li, *Nat. Commun.* **2019**, *10*, 3787.
[18] Y. Zhang, J. Li, Z. Gong, J. Xie, T. Lu, L. Pan, *J. Colloid Interface Sci.* **2021**, *587*, 489.
[19] H. Cheng, L. X. Ding, G. F. Chen, L. L. Zhang, J. Xue, H. H. Wang, *Adv. Mater.* **2018**, *30*, 1803694.
[20] X. Cheng, J. Wang, W. Xiong, T. Wang, T. Wu, S. Lu, G. Chen, S. Gao, X. Shi, Z. Jiang, X. Niu, X. P. Sun, *ChemNanoMat* **2020**, *6*, 1315.
[21] H. Zhu, J. F. Zhang, R. P. Yanzhang, M. L. Du, Q. F. Wang, G. H. Gao, J. D. Wu, G. M. Wu, M. Zhang, B. Liu, J. M. Yao, X. W. Zhang, *Adv. Mater.* **2015**, *27*, 4752.
[22] H. Zhu, G. H. Gao, M. L. Du, J. H. Zhou, K. Wang, B. Wu, X. Chen, Y. Li, P. M. Ma, W. F. Dong, F. Duan, M. Q. Chen, G. M. Wu, J. D. Wu, H. T. Yang, S. J. Guo, *Adv. Mater.* **2018**, *30*, 1707301.

 © 2021 Wiley-VCH GmbH

[23] H. Zhu, L. Gu, D. N. Yu, Y. J. Sun, M. Wan, M. Zhang, L. Wang, L. N. Wang, W. W. Wu, J. M. Yao, M. L. Du, S. Guo, *Energy Environ. Sci.* **2017**, *10*, 321.
[24] X. Wei, M. S. Wang, Y. Bando, D. Golberg, *ACS Nano* **2011**, *5*, 2916.
[25] X. Wei, M. S. Wang, Y. Bando, D. Golberg, *J. Am. Chem. Soc.* **2010**, *132*, 13592.
[26] T. E. Alivio, D. G. Sellers, H. Asayesh-Ardakani, E. J. Braham, G. A. Horrocks, K. E. Pelcher, R. Villareal, L. Zuin, P. J. Shamberger, R. Arróyave, R. Shahbazian-Yassar, S. Banerjee, *Chem. Mater.* **2017**, *29*, 5401.
[27] L. Tian, S. X. Min, F. Wang, *Appl. Catal., B* **2019**, *259*, 118029.
[28] X. M. Yu, P. Han, Z. X. Wei, L. S. Huang, Z. X. Gu, S. J. Peng, J. M. Ma, G. F. Zheng, *Joule* **2018**, *2*, 1610.
[29] Q. Wu, D. Yan, X. F. Li, C. Y. Yu, T. Yao, *Chem. Eng. J.* **2020**, *393*, 123596.
[30] Y. Yoon, A. P. Tiwari, M. Choi, T. Novak, W. Song, H. Chang, T. Zyung, S. S. Lee, S. Jeon, K. S. An, *Adv. Funct. Mater.* **2019**, *29*, 1903443.
[31] J. Zhang, Y. J. Ji, P. T. Wang, Q. Shao, Y. Y. Li, X. Q. Huang, *Adv. Funct. Mater.* **2020**, *30*, 1906579.
[32] L. L. Zhang, M. Y. Cong, X. Ding, Y. Jin, F. F. Xu, Y. Wang, L. Chen, L. X. Zhang, *Angew. Chem., Int. Ed.* **2020**, *59*, 10888.
[33] S. S. Zheng, S. N. Li, Z. W. Mei, Z. X. Hu, M. H. Chu, J. H. Liu, X. Chen, F. Pan, *J. Phys. Chem. Lett.* **2019**, *10*, 6984.
[34] X. Liu, Y. Jiao, Y. Zheng, M. Jaroniec, S. Z. Qiao, *J. Am. Chem. Soc.* **2019**, *141*, 9664.
[35] X. Ren, J. Zhao, Q. Wei, Y. Ma, H. Guo, Q. Liu, Y. Wang, G. Cui, A. M. Asiri, B. Li, B. Tang, X. P. Sun, *ACS Cent. Sci.* **2019**, *5*, 116.
[36] J. H. Kim, Z. Y. Chern, S. Y. Yoo, B. deGlee, J. H. Wang, M. L. Liu, *ACS Appl. Mater. Interfaces* **2020**, *12*, 2370.
[37] S. S. Liu, T. Qian, M. F. Wang, H. Q. Ji, X. W. Shen, C. Wang, C. L. Yan, *Nat. Catal.* **2021**, *4*, 322.

© 2021 Wiley-VCH GmbH